



Electron Microbursts Induced by Nonducted Chorus Waves

Lunjin Chen^{1*}, Xiao-Jia Zhang², Anton Artemyev^{2,3}, Liheng Zheng¹, Zhiyang Xia¹, Aaron W. Breneman⁴ and Richard B. Horne⁵

¹Department of Physics, The University of Texas at Dallas, Richardson, TX, United States, ²Department of Earth, Planetary, and Space Sciences, University of California, Los Angeles, Los Angeles, CA, United States, ³Space Research Institute, RAS, Moscow, Russia, ⁴NASA Goddard Space Flight Center, Greenbelt, MD, United States, ⁵British Antarctic Survey, Cambridge, United Kingdom

OPEN ACCESS

Edited by:

Jean-Francois Ripoll,
CEA DAM Île-de-France, France

Reviewed by:

Chris Colpitts,
University of Minnesota Twin Cities,
United States
Peter Haesung Yoon,
University of Maryland, United States

*Correspondence:

Lunjin Chen
lunjin.chen@gmail.com

Specialty section:

This article was submitted to
Space Physics,
a section of the journal
Frontiers in Astronomy and
Space Sciences

Received: 22 July 2021

Accepted: 13 September 2021

Published: 04 October 2021

Citation:

Chen L,
Zhang X-J, Artemyev A, Zheng L, Xia Z,
Breneman AW and Horne RB (2021)
Electron Microbursts Induced by
Nonducted Chorus Waves.
Front. Astron. Space Sci. 8:745927.
doi: 10.3389/fspas.2021.745927

Microbursts, short-lived but intense electron precipitation observed by low-Earth-orbiting satellites, may contribute significantly to the losses of energetic electrons in the outer radiation belt. Their origin is likely due to whistler mode chorus waves, as evidenced by a strong overlap in spatial correlation of the two. Despite previous efforts on modeling bursty electron precipitation induced by chorus waves, most, if not all, rely on the assumption that chorus waves are ducted along the field line with zero wave normal angle. Such ducting is limited to cases when fine-scale plasma density irregularities are present. In contrast, chorus waves propagate in a nonducted way in plasmas with smoothly varying density, allowing wave normals to gradually refract away from the magnetic field line. In this study, the interaction of ducted and nonducted chorus waves with energetic electrons is investigated using test particle simulation. Substantial differences in electron transport are found between the two different scenarios, and resultant electron precipitation patterns are compared. Such a comparison is valuable for interpreting low Earth-orbiting satellite observations of electron flux variation in response to the interaction with magnetospheric chorus waves.

Keywords: chorus, microbursts, radiation belts, precipitation, wave-particle interaction

1 INTRODUCTION

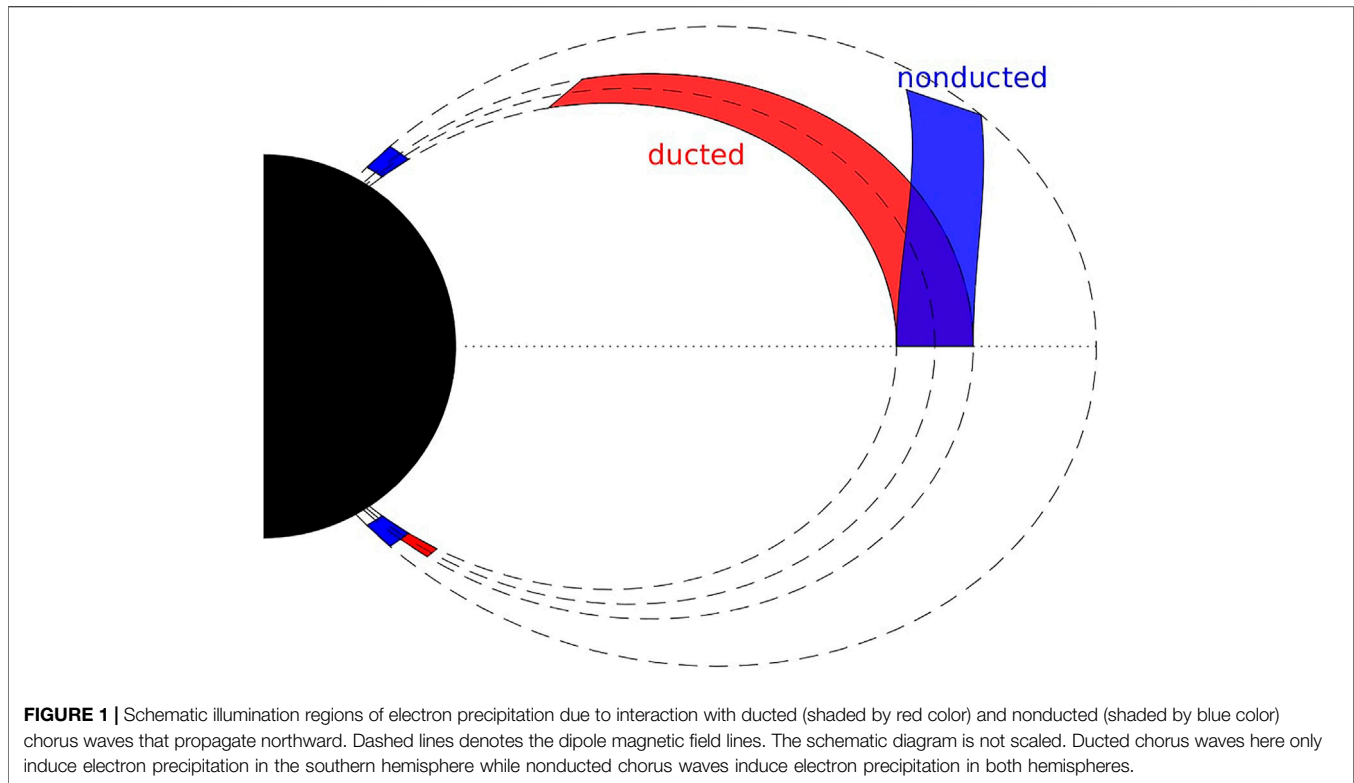
Microbursts are impulsive (typically lasting a few tenths of a second) precipitation of energetic electrons (~30 keV to >1 MeV) from the magnetosphere into the atmosphere. They have been detected indirectly through X-ray counts on balloons (e.g., Anderson and Milton, 1964; Parks et al., 1979; Millan, 2011), and directly through particle detectors onboard rockets (e.g., Lampton, 1967) and low-Earth-orbiting satellites (e.g., Imhof et al., 1992; Douma et al., 2017). Their existence at <100 keV energies has been known for decades, and at higher energies is known only relatively recently. It has been suggested that microburst precipitation into the upper atmosphere may play an important role in radiation belt electron losses (Lorentzen et al., 2001; O'Brien et al., 2004; Millan and Thorne, 2007; Breneman et al., 2017). Recently, bouncing packets in an apparent form of microbursts have been reported by Shumko et al. (2018), suggesting a mixture of precipitating and trapped fluxes in the observation of microbursts (Chen et al., 2020). Blake and O'Brien (2016) discovered that microbursts might not just be temporal bursts of precipitation but may sometimes be very narrow curtain structures of precipitation.

Whistler-mode chorus waves in the Earth's magnetosphere have received great attention because of their dual role in energizing electrons and precipitating them into the lower atmosphere (Horne et al., 2003; Katoh and Omura, 2007; Ni et al., 2011; Reeves et al., 2013; Thorne et al., 2013). Whistler mode waves originate around the magnetic equator, often with nearly field-aligned propagation (e.g., LeDocq et al., 1998; Lauben et al., 2002; Santolík et al., 2005; Li et al., 2009) and they are excited by energetic electrons with anisotropic velocity distribution injected from the magnetotail (e.g., Kennel and Petschek, 1966; Tsurutani and Smith, 1974). Chorus waves often exhibit unique time-frequency spectrograms consisting of discrete rising (or sometimes falling) tones (e.g., Burtis and Helliwell, 1969; Burton and Holzer, 1974; Li et al., 2011a). Numerical theory and simulation studies have demonstrated that nonlinear resonant interactions with a coherent whistler mode wave leads to electron phase trapping, resulting in wave frequency chirping when the background magnetic field is inhomogeneous (Omura and Matsumoto, 1982; Nunn et al., 1997; Katoh and Omura, 2006; Omura and Summers, 2006; Omura et al., 2009; Tao, 2014; Gao et al., 2016). Chorus waves typically occur in the frequency range $0.1\text{--}0.8 f_{ce}$ (f_{ce} is the equatorial electron cyclotron frequency), often separated into distinct lower and upper bands with a wave power gap near $f_{ce}/2$ (e.g., Tsurutani and Smith, 1974; Li et al., 2016a). Statistically, the duration of individual chorus element spectra varies from 0.1 to 1 s, with peak occurrence at ~ 0.4 s at dayside and ~ 0.12 s at nightside (Teng et al., 2017). The spatial scales of individual chorus waves have been unavailable until recently when wave measurements over multiple nearby satellites are present. The estimate of the transverse spatial scale, based on individual event studies, ranges from 7–100 km at $L \sim 4.5$ (Santolík and Gurnett, 2003), ~ 500 km at $L \sim 4.7$ (Shumko et al., 2018), 600–800 km at $L \sim 6$ (Agapitov et al., 2017), to $\sim 3,000$ km in the outer magnetosphere ($L \sim 10$) (Agapitov et al., 2010). The statistical analysis based on 11-years THEMIS wave measurement shows the transverse scale is mostly in the range of $\sim 250\text{--}800$ km over $2 < L < 10$ (Agapitov O. et al., 2018), which is consistent with Shen et al. (2019) results from Van Allen Probes and THEMIS, where the averaged transverse size is ~ 315 km over $5 < L < 6$. These new observational features more thoroughly characterize the temporal and spatial scales of these individual elements, allowing for better modeling of the interaction of chorus waves with energetic electrons.

Whistler-mode chorus waves in the Earth's magnetosphere are suggested to be the primary drivers of relativistic microbursts, creating them by resonant scattering into the loss cone. This association comes from numerous observational and theoretical studies that focus on spatial (L , MLT) (Oliven and Gurnett, 1968; Lam et al., 2010) and temporal similarities (e.g., Lorentzen et al., 2001; Kersten et al., 2011), as well as plausibility of scattering mechanism (to name a few, Chang and Inan, 1983; Rosenberg et al., 1990; Saito et al., 2012; Chen et al., 2020). Statistically, whistler-mode chorus waves are a potential driver of relativistic microbursts (Douma et al., 2017) and the majority of microbursts are shown to have sizes consistent with the sizes of chorus waves (Shumko et al.,

2020). Previous simulation with self-consistent chorus waves (Hikishima et al., 2010) has demonstrated a one-to-one correspondence between microbursts of precipitating electrons and chorus elements. Due to finite transverse scale, individual chorus element will illuminate an area of electron precipitation in the lower atmosphere. Statistically, electron microburst size distribution ranges from 2 to 100 km (Shumko et al., 2020), which is consistent with the size estimate for individual microbursts (Blake et al., 1996; Crew et al., 2016; Shumko et al., 2018), and most occurrences are over a few tens of km, which is about 200 km in size when mapped to the magnetic equator. Such size is comparable to the size of chorus wave packets mentioned above.

The most intense chorus waves are typically confined to within $10\text{--}20^\circ$ of their source near the magnetic equator (e.g., Meredith et al., 2012; Agapitov et al., 2013), while relativistic microbursts (>100 keV) are observed at much higher latitudes (Breneman et al., 2017). Therefore, chorus wave properties at higher latitudes are critically important for modeling microbursts. Depending on wave propagation, the chorus wave intensity off the equator will differ. In the presence of fine-scale density irregularities, chorus waves can be ducted along the field line, with much less attenuated wave intensity away from the equator when compared with the nonducted case in a medium with smoothly varying plasma density. A schematic picture of ducted and nonducted propagation is shown in **Figure 1**. There exists a number of studies on microburst modeling due to the ducted waves (e.g., Hikishima et al., 2010; Saito et al., 2012; Chen et al., 2020), while few focus on the case of nonducted chorus waves. Colpitts et al. (2020) recently showed the first direct observations of individual chorus elements propagating from the equatorial source to higher latitudes, and confirmed with ray tracing that the waves propagated in the nonducted mode. As nonducted chorus waves propagate away from the equator, three important physical processes occur when compared with ducted waves. First, waves experience refraction in the inhomogeneous magnetosphere with wave normal becoming increasingly oblique along the propagation path (e.g., Chen et al., 2013a; Lu et al., 2019; Colpitts et al., 2020). Therefore, oblique whistler-mode mode waves propagate not only along, but also across magnetic field lines. This means that chorus waves at a given field line at high latitude may originate from a different field line at the equator, and thus chorus wave modeling requires the knowledge of their transverse sizes at the equator. Unlike ducted chorus waves, nonducted chorus waves may induce electron precipitation over a broader range of field lines than the range at the equator. Second, chorus waves experience Landau damping as their wave normal angles increase, which will limit the wave intensity at middle latitudes, and high latitudes if accessible (e.g., Chen et al., 2013b; Watt et al., 2013; Colpitts et al., 2020). Third, multiple-harmonics resonances (whose resonance condition is $\omega - k_z v_z = n\Omega/\gamma$ with n being an integer) become effective, when waves becomes oblique and field polarization becomes elliptical (instead of circular), while only the principal resonance ($n = -1$) is effective for ducted



waves. Here ω and k_z are wave angular frequency and parallel component of the wavenumber vector respectively, v_z , Ω and γ are electron parallel velocity, non-relativistic gyrofrequency and Lorentz factor respectively. Thus for northward propagation (as shown in **Figure 1**), nonducted chorus waves could induce electron precipitation in the northern hemisphere (through the resonances with, e.g., $n = 0$ and $+1$) and the southern hemisphere (through the resonance with $n = -1$) while ducted chorus waves could only induce precipitation in the southern hemisphere (through the resonance with $n = -1$). The three physics processes are important for modeling relativistic microbursts due to nonducted chorus waves with oblique wave normal angles (e.g., Artemyev et al., 2016).

In this study, a nonducted chorus wave model is developed as an extension of the ducted chorus wave model (Chen et al., 2020). We will look into the characteristics of electron precipitation due to a nonducted chorus element seen by virtual LEO satellites, which will be compared with that due to a ducted chorus element. In addition to temporal structures, spatial structures of microburst due to the nonducted chorus element will be revealed.

2 TEST PARTICLE MODEL

The dynamics of electrons in a dipole magnetic field with prescribed chorus wave fields is modeled by the following test particle equations along a dipole field line with a given L value (Chen et al., 2020):

$$\frac{dP_z}{dt} = -\frac{\mu}{\gamma} \frac{dB}{dz} + \Sigma_j [q e_{jz} - q v_{\perp} (b_{jx} \sin \theta_g - b_{jy} \cos \theta_g)] \quad (1)$$

$$\frac{dP_{\perp}}{dt} = \frac{\mu}{\gamma} \frac{P_z}{P_{\perp}} \frac{dB}{dz} + \Sigma_j [q v_z (b_{jx} \sin \theta_g - b_{jy} \cos \theta_g) + q (e_{jx} \cos \theta_g + e_{jy} \sin \theta_g)] \quad (2)$$

$$\frac{dz}{dt} = v_z \quad (3)$$

$$\frac{d\theta_g}{dt} = -\Omega/\gamma + \Sigma_j \frac{q}{P_{\perp}} \left[(e_{jy} \cos \theta_g - e_{jx} \sin \theta_g) + v_z (b_{jx} \cos \theta_g + b_{jy} \sin \theta_g) \right] \quad (4)$$

where B is the background dipole magnetic field strength, nonrelativistic electron gyrofrequency $\Omega = \frac{qB}{m}$, magnetic moment $\mu = P_{\perp}^2 / (2mB)$, and q , m , v , P , and γ are electron charge ($q < 0$ for electrons), static mass, velocity, momentum, and Lorentz factor, respectively. The first terms on the right side of **Eqs. 1, 2** represent adiabatic changes due to the background magnetic field, which lead to bounce motion. z , denoting the location of the guiding center along the field line, represents dipole field line arc length with $z = 0$ defined at the equator. The subscripts z and \perp denote directions parallel and perpendicular to the background magnetic field, respectively, while the subscripts x and y denote the radially outward direction and azimuthal direction toward the east, respectively. The set of \hat{x} , \hat{y} and \hat{z} axes constitute the field-aligned coordinate system, a local right-handed Cartesian coordinate system. θ_g is the gyrophase denoting the direction of \mathbf{v}_{\perp} with the respect to the x axis. The subscript j

denotes the j th chorus element with wave electric field \mathbf{e}_j and magnetic field \mathbf{b}_j at the electron's actual location \mathbf{r} . \mathbf{e}_j and \mathbf{b}_j can be represented as $\Re(\tilde{\mathbf{e}}_j e^{i\phi_j(\mathbf{r},t)})$ and $\Re(\tilde{\mathbf{b}}_j e^{i\phi_j(\mathbf{r},t)})$, respectively, where \Re denotes the real part, and $\tilde{\mathbf{e}}_j$ and $\tilde{\mathbf{b}}_j$ are complex amplitudes. These six-component complex amplitudes, which are linearly related, will be scaled by the magnetic field wave amplitude A_w , and the ratio of any two of the six is determined by the linear whistler mode dispersion relation (e.g., Tao and Bortnik, 2010).

Eqs. 1–4 are integrated over a time scale of several electron bounce periods (on the order of 1 s), which is sufficient to describe the interaction between chorus waves and electron gyromotion and to model electron precipitation induced by the chorus waves. Therefore it is safe to neglect drift motion of electrons across magnetic field lines. That is, electrons are trapped by the same field line (with constant L and magnetic local time). Hereafter, we investigate the effect of a single chorus element, either ducted or nonducted, on electron dynamics, and therefore the subscript j and the summation over j will be dropped. For the equations above, gyrophase-averaging on the wave force is not performed, and nonlinear wave particle interaction is included (as the wave phase ϕ depends on z). When test particles reach the atmospheric loss boundary, which is set to an altitude of 100 km, they are considered as lost (precipitated into the upper atmosphere) and no longer traced afterward.

To solve the test particle **Eqs. 1–4** and examine the effect of chorus waves, either ducted or nonducted, on the dynamics of particles at a given field line, it is necessary to find a solution of chorus wave field along that field line (that is, for a given L value in the case of dipole magnetic field). The solution should describe wave phase ϕ and wave amplitude as a function of z and t .

The derivatives of $\phi(\mathbf{r}, t)$ provide definition of wave angular frequency ω and wave normal vector \mathbf{k} through:

$$\frac{\partial \phi}{\partial t} = -\omega(\mathbf{r}, t) \quad (5)$$

$$\frac{\partial \phi}{\partial \mathbf{r}} = \mathbf{k}(\mathbf{r}, t) \quad (6)$$

Given $\omega(\mathbf{r}, t)$ and $\mathbf{k}(\mathbf{r}, t)$, the two equations above can be solved for $\phi(\mathbf{r}, t)$.

$\phi(\mathbf{r}, t)$ can be conveniently rewritten in terms of the guiding center location \mathbf{r}_c as

$$\phi(\mathbf{r}, t) = \phi(\mathbf{r}_c, t) + \mathbf{k}_\perp \cdot \mathbf{r}_{g\perp} \quad (7)$$

where $\phi(\mathbf{r}_c, t)$ is the wave phase at the guiding center \mathbf{r}_c along the field line and the second term on the right denotes the wave phase variation experienced due to the test particle's gyromotion. Oscillatory gyro-radius vector $\mathbf{r}_{g\perp}$, defined as $\mathbf{r} - \mathbf{r}_c$, can be written as $(-\sin \theta_g \hat{\mathbf{x}} + \cos \theta_g \hat{\mathbf{y}}) v_\perp / \Omega$. The term $\mathbf{k}_\perp \cdot \mathbf{r}_{g\perp}$ here is known as the finite Larmor radius effect, which gives rise to harmonic resonances other than $n = -1$. When $k_\perp = 0$ (e.g., for ducted waves), this term vanishes, so do multiple harmonic resonances except $n = -1$.

Initially, test particles are launched at a given L with $N_g (= 120)$ different gyrophases of equal spacing $\Delta\theta_g = 2\pi/N_g$, $N_b (= 120)$ bounce phases of equal spacing $\Delta\phi_b = 2\pi/N_b$, $N_E (= 51)$ energies of

equal logarithmic spacing $\Delta \ln E$ from 50 keV to 1 MeV, and $N_{\alpha_{eq}} (= 66)$ equatorial pitch angles from the equatorial loss cone α_{LC} , which for example is 3.3° at $L = 5.5$, to $\sim 10^\circ$ with a non-equal spacing $\Delta\alpha_{eq}$ (See further explanation below). In total, 4.8×10^7 electrons are traced. For minimizing the discrete nature of the test particle simulation, and thus modeling continuously varying electron flux, each test particle represents a group of ΔN particles located inside the magnetic flux tube of interest and with a range of $\Delta\theta_g$, $\Delta\phi_b$, $\Delta\alpha_{eq}$, and ΔE . Given the initial flux distribution $F_0(\alpha_{eq}, E)$, $\Delta N = F_0 \Delta t \Delta A \Delta E \Delta \Omega'$, where $\Delta \Omega' = \sin \alpha \Delta \alpha \Delta \theta_g$ (α is the local pitch angle), $\Delta A = \Delta A_\phi / \cos \alpha$, $\Delta t = \Delta \phi_b / \omega_b$ (ω_b is electron bounce angular frequency), and $\Delta E = E \Delta \ln E$. The cross section area of the magnetic flux tube (a constant magnetic flux $\Delta \Phi_m$) $\Delta A_\phi = \Delta \Phi_m / B$. Virtual LEO satellites are placed at the southern and northern footpoints of the field line L at a given altitude of 650 km. Electron fluxes at these footpoints as a function of pitch angle, energy and time t are reconstructed from the test particle results of those 4.8×10^7 electrons. To better model the electron flux variations at the LEO satellite locations as a function of pitch angles, a non-equal spacing $\Delta\alpha_{eq}$ is used so that sufficient number of α_{eq} grids covers both the following two α_{eq} ranges, one from the equatorial loss cone α_{LC} to the value of $\alpha_{eq\text{mirror}}$ corresponding to the mirroring location at the LEO altitude and the other one from $\alpha_{eq\text{mirror}}$ to $\sim 10^\circ$. Following Chen et al. (2020), we adopt an anisotropic initial distribution as $F_0 = F_{0E}(E) \sin \alpha_{eq}^2$, where the energy dependent $F_{0E}(E)$ is obtained from the Van Allen Probes flux observation at pitch angle 90° shown in **Figure 2** of Breneman et al. (2017). Such simplified adoption of the electron anisotropy may affect the magnitude of electron fluxes, but is not critical for addressing general characteristics of electron flux variations.

3 DUCTED CHORUS WAVES

Ducted chorus waves are guided along a field line, say L_c , by keeping wavevector parallel or antiparallel to the field line. During ducted propagation, chorus waves follow:

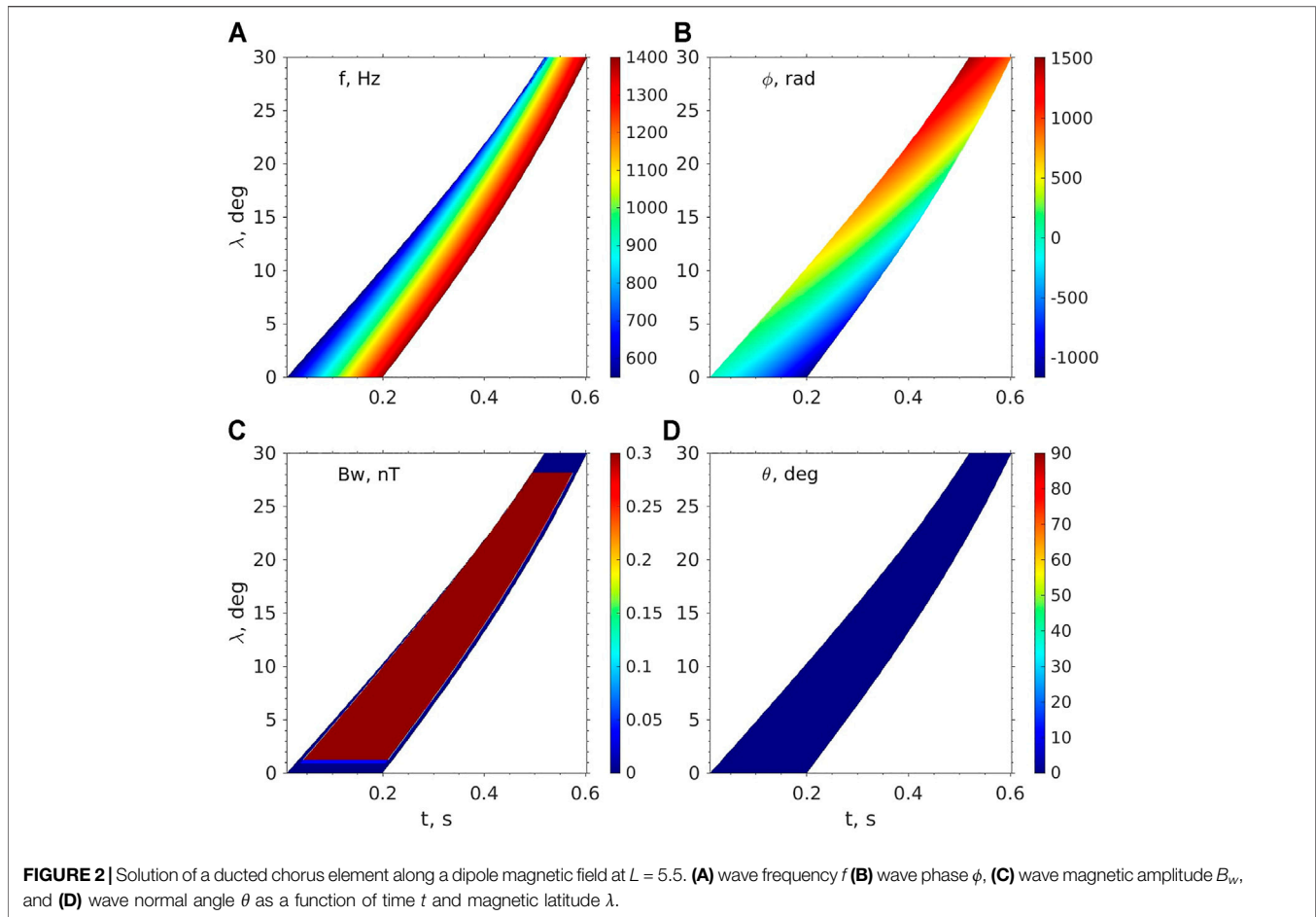
$$\mathbf{k}_\perp = 0 \quad (8)$$

$$D(k_z, \omega, z) = 0 \quad (9)$$

$$\frac{\partial \omega}{\partial t} + v_{gz} \frac{\partial \omega}{\partial z} = 0 \quad (10)$$

$$\frac{\partial A_w}{\partial t} + v_{gz} \frac{\partial A_w}{\partial z} = 0 \quad (11)$$

where the first equation describes the constraint of parallel propagation, the second equation describes the local dispersion relation D , which adopts one for whistler mode in the cold plasma at the location z , and the third and fourth equations state the conservation of wave frequency and wave amplitude along the propagation path. The parallel component of group velocity $v_{gz} = -(\partial D / \partial k_z) / (\partial D / \partial \omega)$. These equations, assuming parallel propagation, have been widely used for chorus wave modeling (e.g., Furuya et al., 2008; Tao et al., 2012; Chen et al., 2020). For such "ideally" ducted propagation ($\mathbf{k}_\perp = 0$), it is implicitly assumed



that there exists a density duct with density gradients that perfectly overcome wave refraction due to magnetic field inhomogeneity. This implicit assumption places a constraint on the density gradients of the duct, whose solution, fortunately, is not required for modeling the ideally ducted propagation. For a more realistic ducted propagation (a non-ideal case, e.g., Liu et al., 2021), wave normal direction would experience oscillation near the parallel direction and so ducted ray paths.

Let $\omega_0(t)$ be the prescribed chorus wave frequency-time profile in the equatorial source region. Then the one-sided boundary condition at the equator can be provided as

$$\omega(z = 0, t) = \omega_0(t). \quad (12)$$

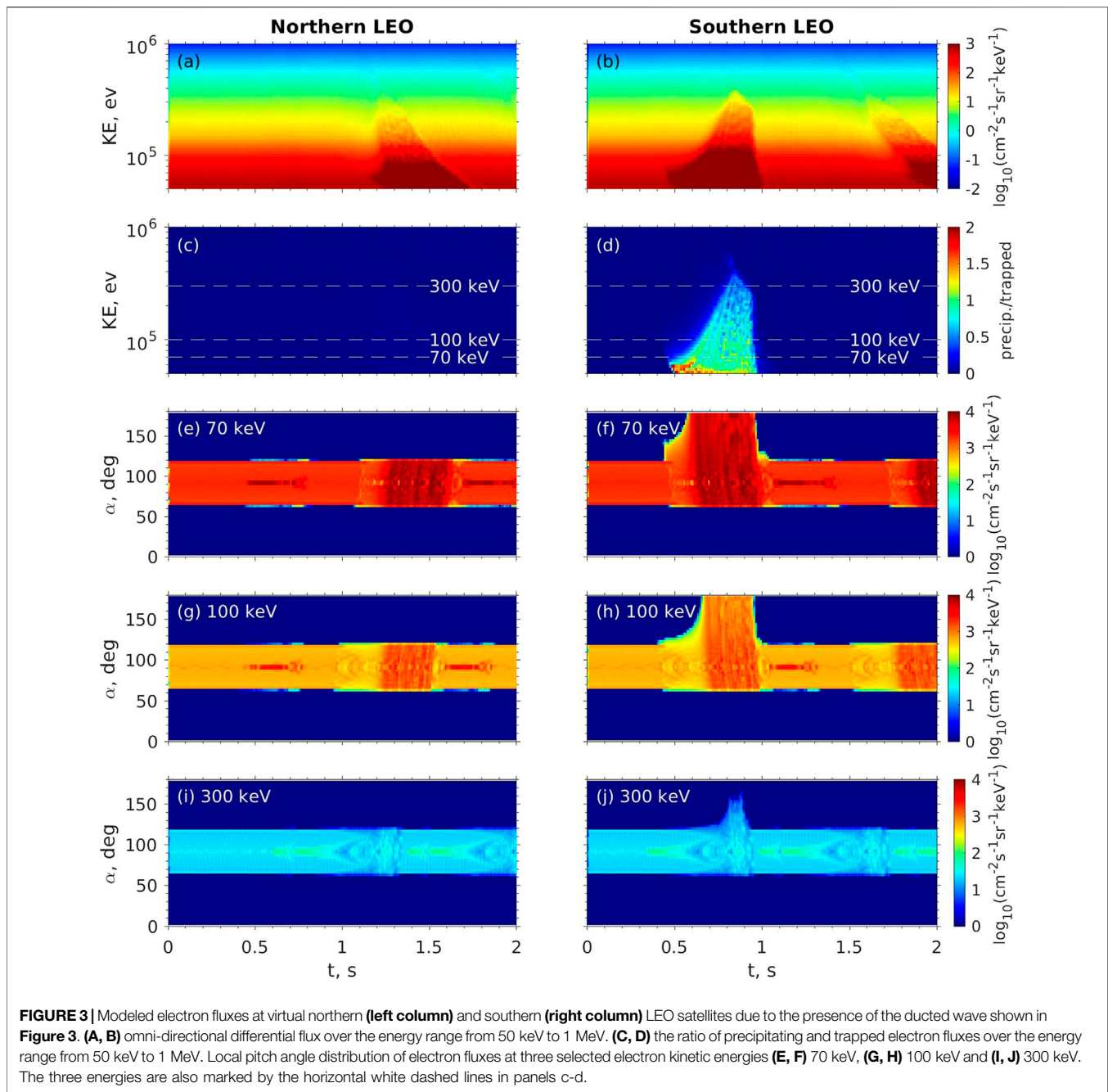
Equations 10–12 can be solved for $\omega(z, t)$ using the method of characteristics (e.g., Furuya et al., 2008; Tao et al., 2012). With $\omega(z, t)$ solved, **Eq. 9** yields the solution of $k_z(z, t)$. Then the solution of wave phase $\phi(z, t)$ can be numerically integrated by the following two constituent equations:

$$\frac{\partial \phi}{\partial t} = -\omega(z, t) \quad (13)$$

$$\frac{\partial \phi}{\partial z} = k_z(z, t) \quad (14)$$

For the calculation of the dispersion relation (D in **Eq. 9**), background plasma density is required. We adopt the modified diffusive equilibrium density model (Bortnik et al., 2011). The same initial condition $\omega_0(t)$ as Chen et al. (2020) is used, with the wave frequency f rising from 550 to 1,400 Hz over an interval of 0.2 s. The solution of wave frequency and wave phase is shown in **Figures 3A,B**. At $\lambda = 0$, wave frequency chirps over a duration of 0.2 s, while as λ increases, the wave duration becomes shorter due to frequency dispersion. In **Figure 3B**, wave phase ϕ increases with λ and decreases with t , as shown by **Eqs. 13, 14**. The wave normal angle θ is zero, as expected (**Figure 3D**).

To represent a chorus element of a flexible amplitude, the initial amplitude profile is implemented as $A_{w0}(f, \lambda) = A_{w,max}G(f; f_1, f_2, \delta f_1, \delta f_2)$, where λ is magnetic latitude and $A_{w,max}$ is the maximum wave amplitude. The function G has a Gaussian-like profile with a flat-top and four control parameters ($x_1, x_2, \delta x_1, \delta x_2$). Specifically, $G(x; x_1, x_2, \delta x_1, \delta x_2)$ is defined as $\exp(-(x - x_1)^2 / \delta x_1^2)$ for $x < x_1$, $= \exp(-(x - x_2)^2 / \delta x_2^2)$ for $x > x_2$, with values equal to unity for $x_1 \leq x \leq x_2$. Further explanation on the G function can be found in the **Supplementary Material**. We set $A_{w,max} = 300$ pT (corresponds to intense chorus waves in the radiation belts (e.g., Agapitov O. V. et al., 2018; Zhang et al., 2018;



Tyler et al., 2019)), $f_1 = 600$ Hz, $f_2 = 1,350$ Hz, $\delta f_1 = 10$ Hz, and $\delta f_2 = 10$ Hz. With A_w given, Eq. 11 is solved for A_w . To represent latitudinal characteristics for field-aligned propagating chorus waves, an additional factor of a latitudinal profile of the wave amplitude is added as $G(\lambda; \lambda_1, \lambda_2, \delta\lambda_1, \delta\lambda_2)$, with $\lambda_1 = 1^\circ$, $\lambda_2 = 28^\circ$, $\delta\lambda_1 = 0.1^\circ$, and $\delta\lambda_2 = 0.1^\circ$. Using the prescribed amplitude profile and the obtained wave phases, complex amplitudes of the six electromagnetic components can be obtained and then test particle equations above can be solved.

Figure 3C shows the solution for the ducted chorus wave amplitude. The wave amplitude B_w is nearly constant in the $z-t$ regime of the chorus wave field, expect the lower and higher latitude boundaries due to the introduced latitude-dependence term $G(\lambda; \lambda_1, \lambda_2, \delta\lambda_1, \delta\lambda_2)$ and the lower and higher time boundaries due to the frequency-dependence term $G(f; f_1, f_2, \delta f_1, \delta f_2)$. The introduction of the latitude-dependence term mimics the chorus growth near the equator and ensures the test particles are launched before the chorus

wave field perturbation occurs, and the test particles, if not reaching the atmospheric loss boundary, are terminated after the chorus wave field perturbation ends. By doing so, the effect of chorus wave field perturbation on electron flux can be evaluated.

Figure 2 shows modeled electron distribution at two virtual LEO satellites, which are placed at northern and southern foot points of $L = 5.5$ at 500 km altitude. The electrons accessing these locations are reorganized to obtain the full velocity distribution as a function of t at the two locations, respectively. The distribution is then used to calculate derived quantities, such as omni-directional differential flux, precipitating flux (the averaged flux over the solid angle within the loss cone), and trapped flux (the averaged flux over the solid angle beyond the loss cone). **Figures 2A,B** shows the omni-directional differential flux at the two, northern and southern, LEO satellite locations. One can see flux enhancement with energy from 50 up to 400 keV. The flux enhancement first appears 0.5–1 s at the southern location (**Figure 2B**), then over 1.2–1.7 s at the northern location (**Figure 2A**), and then again near 1.7 s at the southern location (**Figure 2B**). Such a series have been identified previously (e.g., Chen et al., 2020) as bouncing microburst packet. The initial flux enhancement is caused by cyclotron resonance of southward moving electrons with a northward propagating chorus element, which leads to a net transport towards smaller pitch angle. To resonate with the northward propagating chorus wave, electrons must be counter-moving to the south in order to satisfy the Doppler-shifted resonance condition with $n = -1$. Such initial flux enhancement occurs for both precipitating flux and trapped flux near 0.5–1 s in the southern hemisphere (**Figure 2D**). The subsequent flux enhancements, which corresponds to enhanced trapped flux only (**Figures 2C,D**), is caused by bounce motions of the enhanced trapped flux in the initial flux enhancement (See more detailed explanation on electron bouncing packets in Chen et al. (2020)). The ratio of precipitating to trapped flux is only significant in the southern location during the initial enhancement. The ratio decreases for higher energy, from as high as 2 at 50 keV, near 1 at 100 keV, and to a fraction near 300 keV (**Figure 2D**). The ratio exceeding unity at the low energy demonstrates nondiffusive transport in pitch angle, as a signature of nonlinear wave-particle interaction (Chen et al., 2020). **Figures 2E–J** shows the pitch angle distribution of electron unidirectional different flux at 70 keV, 100 and 300 keV. One can see full loss cone distribution (at electron energy, e.g., 70 keV in **Figure 2F** and 100 keV in 3 h) when the ratio of precipitating to trapped flux is 1 and above while partial loss cone corresponds to the case with the ratio being a fraction (at electron energy, e.g., 300 keV in **Figure 2J**). As expected, the ratio is zero for a completely empty loss cone. The simultaneous enhancement of trapped flux and precipitating flux (**Figures 2F,H,J**) is caused by the induced transport from the larger α_{eq} into the loss cone. Although short-lived, the chorus element can produce the permanent change to trapped electron distribution via bouncing packets, in addition to impulsive precipitation.

4 NONDUCTED CHORUS WAVES

An extension is made from the ducted chorus wave case to the case allowing nonducted propagation of chorus waves across magnetic field lines. Nonducted propagation is modeled by solving the following ray tracing equations (e.g., Horne, 1989):

$$\frac{d\mathbf{r}}{dt} = -\frac{\partial D}{\partial \mathbf{k}} / \frac{\partial D}{\partial \omega} \quad (15)$$

$$\frac{d\mathbf{k}}{dt} = \frac{\partial D}{\partial \mathbf{r}} / \frac{\partial D}{\partial \omega} \quad (16)$$

$$\frac{d\omega}{dt} = 0 \quad (17)$$

$$\frac{dA_w}{dt} = \gamma_L A_w \quad (18)$$

where $D(\mathbf{k}, \omega, \mathbf{r}) = 0$ is the local dispersion relation, the right-handed side of the first equation is the general definition of the wave group velocity \mathbf{v}_g , and the fourth equation for wave amplitude A_w takes into account wave attenuation as a result of Landau damping due to the suprathermal electron population during oblique propagation. The suprathermal electron model used is based on THEMIS statistical observations of electron distribution over the energy range from ~ 0.1 to 26 keV (see detail in **Section 3** of Chen et al., 2013a). The ray tracing HOTRAY code (Horne, 1989) is used to calculate the nonducted propagation paths of whistler mode waves in a smoothly-varying plasma, and to evaluate the path integrated gain, which represents the relative change of wave amplitude. The ray tracing method assumes that the spatial scales of the medium, notably the plasma density and magnetic field, are large compared to the wavelength, and that their spatial gradients remain continuous. Like **Section 3**, the diffusive equilibrium density model (Bortnik et al., 2011) is used.

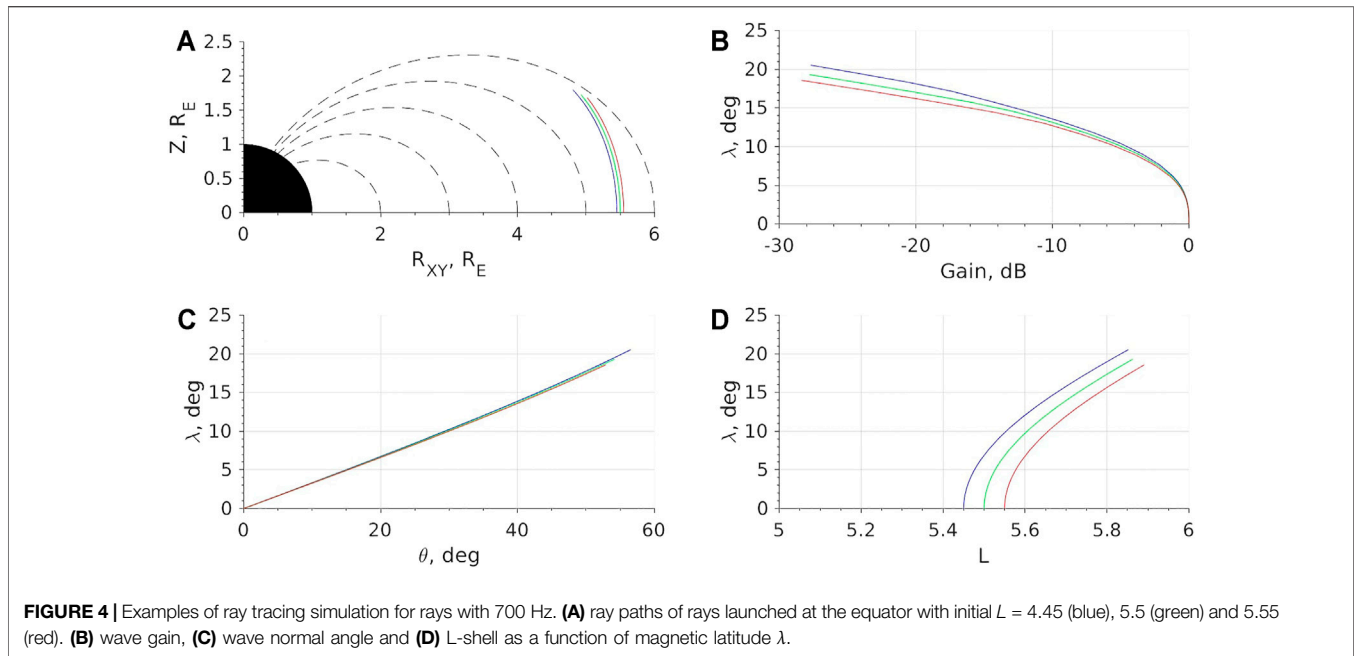
Say a ray with frequency ω_0 is launched at a source location \mathbf{r}_0 and initial wave vector \mathbf{k}_0 at time t_0 . The ray is labeled by the set of initial parameters $(\omega_0, t_0, \mathbf{r}_0, \mathbf{k}_0)$, subject to two constraints. First, the launch time t_0 depends on ω_0 according to the prescribed chorus frequency-time profile at the source location \mathbf{r}_0 . Second, the local dispersion relation is satisfied initially, $D(\mathbf{k}_0, \omega_0, \mathbf{r}_0) = 0$. The ray tracing equations are solved numerically; the solution can be obtained: $\omega = \omega_0$, and symbolically $\mathbf{r} = \mathbf{r}(t; \omega_0, t_0, \mathbf{r}_0, \mathbf{k}_0)$, $\mathbf{k} = \mathbf{k}(t; \omega_0, t_0, \mathbf{r}_0, \mathbf{k}_0)$, and $A_w = A_w(t; \omega_0, t_0, \mathbf{r}_0, \mathbf{k}_0)$, subject to the constraint $D(\mathbf{k}, \omega, \mathbf{r}) = 0$.

It should be noted that the solution of $\mathbf{r} = \mathbf{r}(t; \omega_0, t_0, \mathbf{r}_0, \mathbf{k}_0)$ provides characteristic curves (ray paths) for the following two equations for ω and A_w

$$\frac{\partial \omega}{\partial t} + \mathbf{v}_g \cdot \frac{\partial \omega}{\partial \mathbf{r}} = 0 \quad (19)$$

$$\frac{\partial A_w}{\partial t} + \mathbf{v}_g \cdot \frac{\partial A_w}{\partial \mathbf{r}} = \gamma_L A_w. \quad (20)$$

The two equations are equivalent to **Eqs. 17, 18**, with the directive derivative $d/dt = \frac{\partial}{\partial t} + \mathbf{v}_g \cdot \frac{\partial}{\partial \mathbf{r}}$. With the aid of **Eqs. 5, 6**, ϕ along the ray path $\mathbf{r} = \mathbf{r}(t; \omega_0, t_0, \mathbf{r}_0, \mathbf{k}_0)$ can be obtained as



$$\phi(t; \omega_0, t_0, \mathbf{r}_0, \mathbf{k}_0) = \phi_0 + \int_{\text{raypath}} \mathbf{k} \cdot d\mathbf{r} - \omega(t - t_0), \quad (21)$$

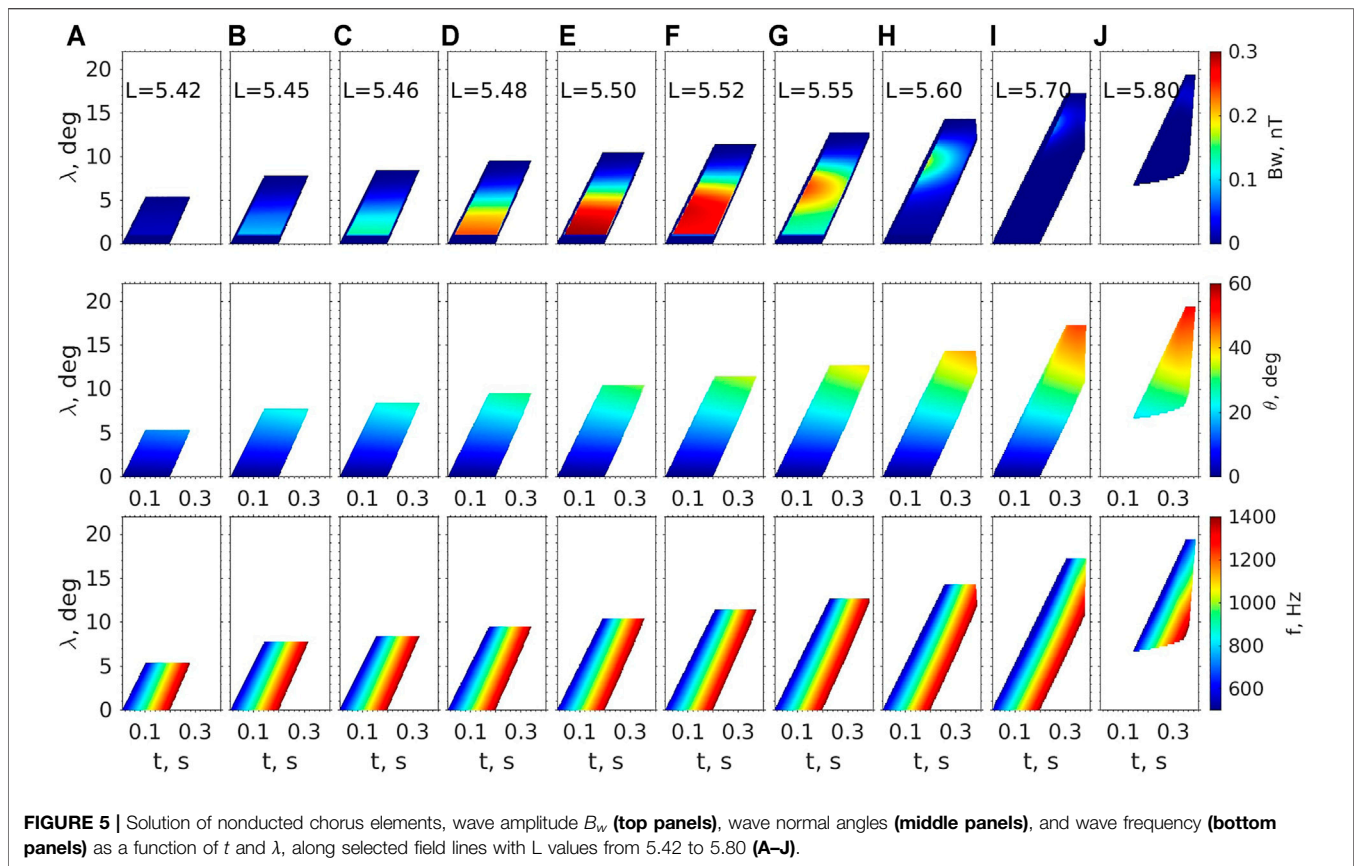
where $\phi_0 = \phi_0(t_0, \mathbf{r}_0)$ is the initial phase at \mathbf{r}_0 and at $t = t_0$. The solution of A_w can be written in an alternative fashion as

$$A_w(t; \omega_0, t_0, \mathbf{r}_0, \mathbf{k}_0) = A_{w0} \exp\left(\int_{\text{raypath}} \gamma_L dt\right), \quad (22)$$

where $A_{w0} = A_{w0}(t_0, \mathbf{r}_0)$ is the initial amplitude at \mathbf{r}_0 and at $t = t_0$.

For 3D space in \mathbf{r} , the initial conditions A_{w0} and ϕ_0 over a 2D spatial area (spanned by \mathbf{r}_0) of the wave source are needed as input. For a simpler case of 2D propagation on the meridian plane at a fixed local time, the initial conditions over a 1D curve (spanned by \mathbf{r}_0) of the wave source are needed. Hereafter we will limit the nonducted propagation on a meridian plane. Let us consider a chorus element at the equator at magnetic local time (MLT) of 6 h with wave amplitude peak at a L-shell value of $L_c = 5.5$ and a Gaussian width of $\delta L = 0.05 R_E$ (corresponding to 320 km). The chosen location is consistent with the location of the microburst occurrence rate peak during geomagnetic active conditions (Douma et al., 2017) and the choice of the δL value is consistent with the mean spatial width of chorus wave elements (Shen et al., 2019). The source wave amplitude $A_{w0}(f, L_0) = A_{w,max} \times G(f, f_1, f_2, \delta f_1, \delta f_2) \times G(L_0, L_c, L_c, \delta L, \delta L)$. Without the loss of generality, the initial wave phase ϕ_0 is set to 0. To ensure sufficient chorus rays, we use 51 launch locations with L_0 from 5.25 to 5.75 in the spacing of 0.01 and 81 frequencies f from 600 to 1,400 Hz with spacing of 10 Hz. In total, 4,131 ray paths (characteristic curves) are traced. ϕ , A_w , and \mathbf{k} along those paths are interpolated to reconstruct the corresponding 3D distributions in time t and position \mathbf{r} (on the meridian plane), which are then fed into the test particle Eqs. 1–4.

Figure 4 shows examples of three rays launched at the equator on different field lines. As the rays propagate away from the equator, wave normals refract outward due to the dipole magnetic field (**Figure 4C**), i.e., \mathbf{k}_\perp is pointed outward during wave propagation. Whether whistler-mode ray paths bend outward or inward depends on perpendicular wave group velocity ($\mathbf{v}_{g,\perp}$) direction (e.g., Smith et al., 1960), which depends on wave frequency and wave normal angle. For $\omega > \Omega/2$, $\mathbf{v}_{g,\perp}$ is always anti-parallel to \mathbf{k}_\perp and thus is pointed inward. For $\omega < \Omega/2$, when the wave normal angle is smaller (larger) than the Gendrin angle, the $\mathbf{v}_{g,\perp}$ direction is parallel (anti-parallel) with \mathbf{k}_\perp , which corresponds to outward (inward) bending of ray paths. Therefore, ray paths of the lower band chorus waves with initially parallel wave normal at the equator generally bend outward and toward larger L (as shown in **Figures 4A–D**). As wave normal increases, so does Landau damping. At the latitude of 20° , wave normal angles reach above 50° and path-integrated gain reaches below -20 dB. The same features can be also seen in the solution of nonducted chorus wave amplitude and wave normal angles as shown in **Figure 5**. In addition, chorus wave intensity is maximized at $L = 5.5$ near the equator, as chorus wave propagates outward, wave intensity peak is weakened and shifts toward higher latitude with more oblique wave normal angles. During wave propagation away from the equator, the nonducted chorus wave can extend to a higher L -shell, beyond the transverse range at the equator, and consequently is capable of interacting with electrons over a larger L range than the ducted chorus wave. However, due to Landau damping, the nonducted chorus wave intensity is mostly confined over $\lambda < 20^\circ$ and $L < 5.8$. It is also noted that the chorus wave above $\lambda \sim 10^\circ$ is available only beyond $L = 5.5$ because of the outward propagation of wave energy and the limited chorus transverse size, while the chorus wave is

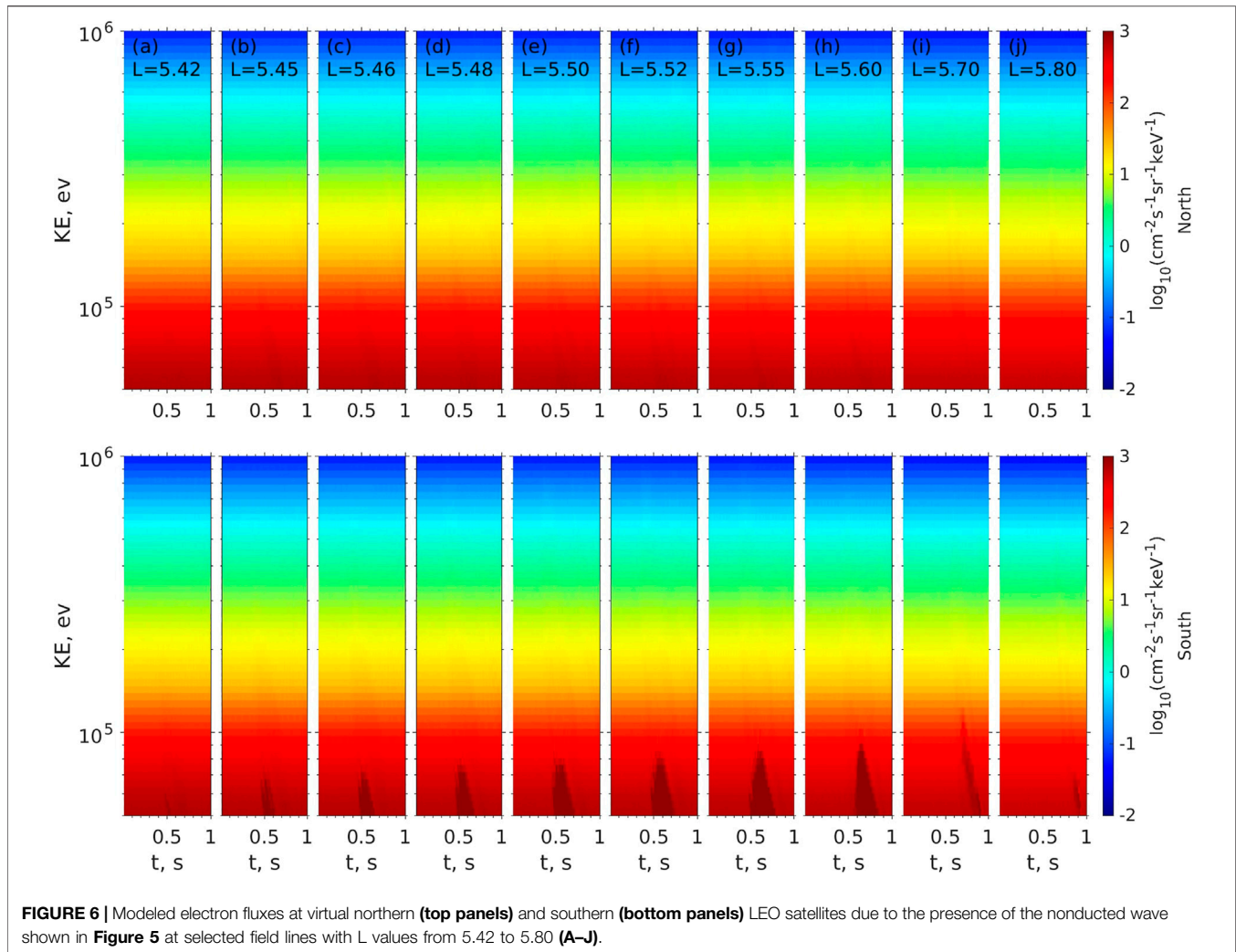


confined near the equator near $L \sim 5.5$. Bottom panels of **Figure 5** show the corresponding solution for wave frequency. One can see frequency chirping evolve as chorus waves propagate away from the equator.

Figure 6 shows the response of electron omni-directional fluxes at the two LEO satellite locations along different L values (represented by different columns). Due to the tendency of outward propagation of nonducted chorus waves, the responses are asymmetric with respect to the central location L_c of the equatorial chorus wave source, with more pronounced flux enhancement over a broader energy range outside L_c than inside L_c . The chorus waves are capable of inducing electron responses at the southern footpoints over a L range from 5.45 to 5.7, a factor of 5 greater than the transverse size δL ($= 0.05$) of the equatorial chorus waves. The perturbation of the omni-directional flux is hardly visible in the northern footpoints. The corresponding ratios of precipitating to trapped electron fluxes are shown in **Figure 7**. The ratios at the southern footpoints can be on the order of 1 over the energy range of 50–70 keV over the L range from 5.45 to 5.6. For higher energy range, the ratios becomes smaller and the corresponding L range becomes narrower. Such enhancement in electron precipitation at the southern hemisphere is induced by the principal cyclotron resonance ($n = -1$) with the chorus waves. At the northern footpoints, the enhanced electron precipitating-to-trapped

flux ratios are on the order of 0.01–0.1 at the outer L -shell with $L > 5.5$, which was caused by anomalous cyclotron resonance with $n = +1$ (requiring northward moving electrons). The anomalous cyclotron resonance requires significant wave intensity at oblique angles, and therefore favors the outer L shells. These ratios are lower than those associated with the $n = -1$ resonance because the intensity of the oblique waves is less than that of the equatorial waves. **Figure 8** shows pitch angle distribution of electron fluxes at a selected energy 70 keV. One can see partial and full loss cone (over the local pitch angle range from 118° to 180°) at the southern footpoints over the L range where chorus wave intensity remains strong, while at the northern footpoints, the loss cone in the pitch angle range below 62° is only slightly filled. The comparison of those pitch angle distributions is consistent with the precipitating-to-trapped flux ratio values shown in **Figure 7**.

The following four points are worth-noting when making comparison between ducted chorus waves and nonducted chorus waves. First, ducted chorus waves are capable of reaching higher latitude than nonducted chorus waves, and therefore are capable of inducing the electron precipitation at higher energy. Second, nonducted chorus waves can spread wave energy toward outer L -shell and becomes more oblique. Therefore, the electron precipitation, although at lower energy, will be induced over a spatial region a factor of

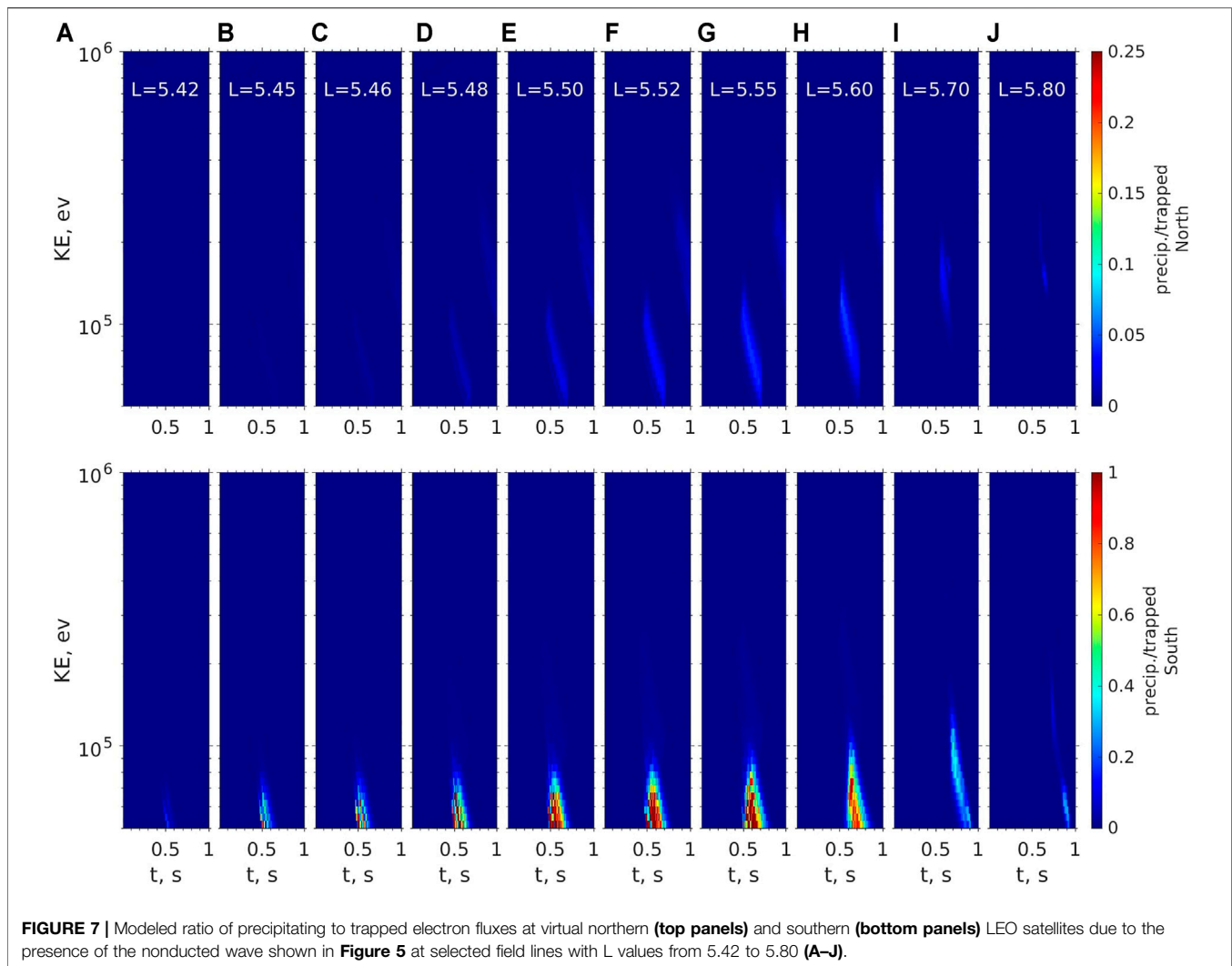


several larger than the size of source chorus waves at the equator. Third, because of obliqueness, nonducted chorus waves introduce additional anomalous cyclotron resonance, as well as many higher order resonances that are generally less effective in electron scattering for moderately oblique waves (e.g., Shprits and Ni, 2009). The degree of outward propagation and wave obliqueness depends on the strength of Landau damping, which increases with L and Kp index and which is greater at nightside than dayside (Chen et al., 2013b). For a strong Landau damping case (such as nightside), one may expect more confinement of chorus waves at the equator, narrower L -shell spreading, less anomalous cyclotron resonance effect, and electron precipitation at lower energy. On the other hand, for a weak Landau damping case (such as morning side), one may expect more wave energy at higher latitudes, and spreaded wave intensity over a broader L range, electron precipitation at higher energy, and more significant anomalous cyclotron resonance effect. One can see the effects of the reduced Landau damping by comparing

Figure 7 with **Supplementary Figure S2** of **Supplementary Material**, where the Landau damping rate γ_L is halved. Fourth, for a given energy, nonducted chorus waves tend to introduce a narrower microburst duration compared with the ducted waves. That is because nonducted chorus waves at any given frequency only retain wave energy at a given L over a latitudinal range much narrower than the ducted waves along the same field. This reason also explains the difference in the energy dispersion of electron microbursts due to the ducted (**Figure 2B**) and nonducted chorus waves (**Figure 6**).

5 CONCLUSION AND DISCUSSION

We model electron flux response (including trapped and precipitating electrons) due to ducted and nonducted chorus elements and make comparison of the induced electron precipitation between the two cases. Our principal conclusions are summarized as follows:

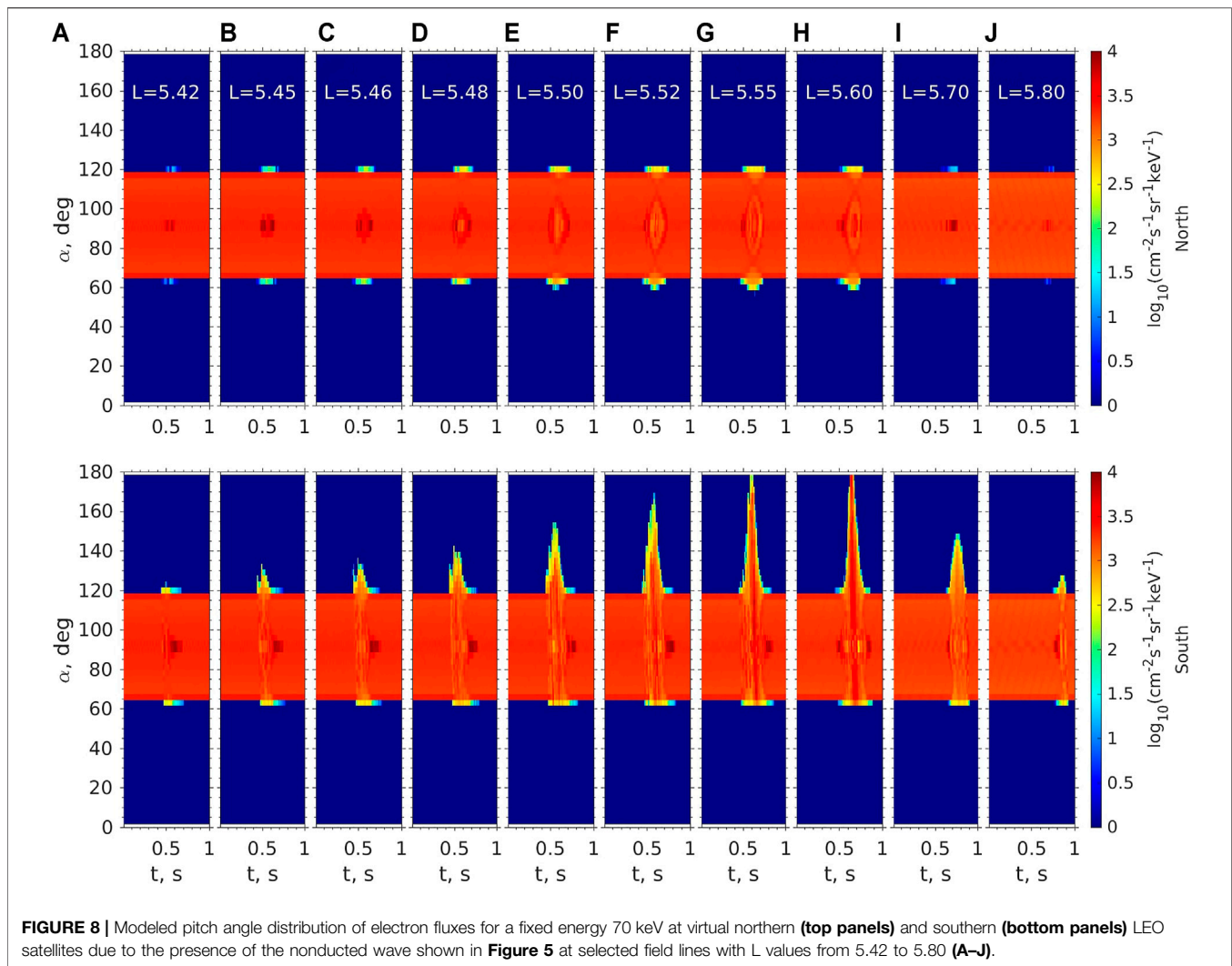


- A dynamic model of nonducted chorus propagation is developed. In comparison with ducted chorus, nonducted chorus tends to be more confined near the equator, with wave energy decaying and propagating outward while propagating away from the equator.
- A numerical model of electron flux variation to nonducted chorus elements is developed. Such a model is valuable when interpreting the cause of microburst flux and predicting electron flux variation at a virtual observation.
- Distinct electron precipitation patterns due to the nonducted chorus waves are identified. Comparing with ducted chorus waves, nonducted waves tend to produce electron microbursts at lower energy, over a shorter duration, and over a broader L -shell region, and can trigger different resonance mechanisms (in addition to the principal resonance with $n = -1$).

There exist three factors that affect nonducted wave propagation and wave intensity. First, Landau damping

shows strong dependence on L and MLT and K_p (Chen et al., 2012). Severe Landau damping limits the chorus wave intensity at high latitude and reduces the obliqueness of chorus waves. Second, wave propagation depends on the background plasma density variation, such as strong density gradient near the plasmapause. Third, the transverse size δL of equatorial chorus waves is another important factor. For a larger size, the off-equatorial chorus waves can obtain higher intensity. One can see the effects of increased δL by comparing **Figure 7** with **Supplementary Figure S3 of Supplementary Material**, where δL is doubled.

Our study is limited to the case of nonducted propagation on the meridian plane here. Whistler waves have been shown to be confined near a meridian plane except there exists strong azimuthal density gradient such as near the plasmapause or near the plume region. When needed for those cases, our model is capable of extending to a more general three spatial-dimension case. The presented comparison of microburst characteristics due to ducted and nonducted



chorus waves will be valuable when interpreting the LEO observation of microburst structures. Our model is capable of revealing both temporal and spatial structures of induced electron precipitation.

The Landau damping can be significantly reduced by field-aligned electron beams or plateaus (see Ma et al., 2017) that are frequently observed around chorus generation regions (probably as an ionospheric response to electron precipitation by whistler waves, see Nishimura et al. (2015); Artemyev and Mourenas (2020)). Such reduced damping is associated with observations of very oblique chorus waves around the equatorial plane (e.g., Agapitov et al., 2016; Li et al., 2016b) and at middle latitudes Agapitov et al. (2013). The presented model results suggest that very oblique wave generation and propagation without significant damping also may generate microburst precipitation. Further simulations and model comparison with low-altitude spacecraft measurements will be required to reveal relative contributions of electron losses by different chorus wave modes (ducted waves, nonducted moderately and strongly oblique waves) for different electron

energy ranges and geomagnetic conditions. To assess overall contribution of chorus waves to the radiation belt losses, relative occurrences of different chorus wave modes should be quantified separately, which is left for future exploration.

Finally, the development of nonducted chorus wave model, which is based on the solution of ray tracing, can be applied to model other coherent plasma waves, such as whistler waves due to lightning activities and from ground transmitter signals. The wave model allows flexible input on initial wave properties, and therefore is ideal for modeling a specific event with constraint by the observation. The general test particle equations can be used for modeling the effect of nonlinear wave particle interaction over a time scale of bounce periods. Results of such short-term simulation can be generalized for a long-term evolution due to nonlinear wave-particle interaction, by including test particle results into the modified Fokker-Planck equation describing phase trapping as a probabilistic process through the Green function approach (e.g., Omura et al., 2015), nonlocal transport operator (e.g., Artemyev et al., 2018), or the Markov chain method (e.g., Zheng et al., 2019).

DATA AVAILABILITY STATEMENT

No observational data were used in this study. Figure data are available at <https://doi.org/10.5281/zenodo.5123390>.

AUTHOR CONTRIBUTIONS

LC proposed the research idea, ran the simulation, and wrote the article. XZ and AA improved the idea and provided consultation on the interaction with ducted and nonducted chorus waves. LZ and ZX assisted with 1D and 2D chorus wave models. AB provided consultation on electron microbursts. RH developed the HOTRAY code and instructed its usage. All authors reviewed the article.

REFERENCES

- Agapitov, O., Artemyev, A., Krasnoselskikh, V., Khotyaintsev, Y. V., Mourenas, D., Breuillard, H., et al. (2013). Statistics of Whistler Mode Waves in the Outer Radiation Belt: Cluster STAFF-SA Measurements. *J. Geophys. Res. Space Phys.* 118, 3407–3420. doi:10.1002/jgra.50312
- Agapitov, O., Blum, L. W., Mozer, F. S., Bonnell, J. W., and Wygant, J. (2017). Chorus Whistler Wave Source Scales as Determined from Multipoint Van Allen Probe Measurements. *Geophys. Res. Lett.* 44, 2634–2642. doi:10.1002/2017GL072701
- Agapitov, O., Krasnoselskikh, V., Zaliznyak, Y., Angelopoulos, V., Le Contel, O., and Rolland, G. (2010). Chorus Source Region Localization in the Earth's Outer Magnetosphere Using THEMIS Measurements. *Ann. Geophys.* 28, 1377–1386. doi:10.5194/angeo-28-1377-2010
- Agapitov, O., Mourenas, D., Artemyev, A., Mozer, F. S., Bonnell, J. W., Angelopoulos, V., et al. (2018a). Spatial Extent and Temporal Correlation of Chorus and Hiss: Statistical Results from Multipoint Themis Observations. *J. Geophys. Res. Space Phys.* 123, 8317–8330. doi:10.1029/2018JA025725
- Agapitov, O. V., Mourenas, D., Artemyev, A. V., and Mozer, F. S. (2016). Exclusion Principle for Very Oblique and Parallel Lower Band Chorus Waves. *Geophys. Res. Lett.* 43, 112–120. doi:10.1002/2016GL071250
- Agapitov, O. V., Mourenas, D., Artemyev, A. V., Mozer, F. S., Hospodarsky, G., Bonnell, J., et al. (2018b). Synthetic Empirical Chorus Wave Model from Combined Van Allen Probes and Cluster Statistics. *J. Geophys. Res. Space Phys.* 123, 297–314. doi:10.1002/2017ja024843
- Anderson, K. A., and Milton, D. W. (1964). Balloon Observations of X Rays in the Auroral Zone: 3. High Time Resolution Studies. *J. Geophys. Res.* 69, 4457–4479. doi:10.1029/JZ069i021p04457
- Artemyev, A., Agapitov, O., Mourenas, D., Krasnoselskikh, V., Shastun, V., and Mozer, F. (2016). Oblique Whistler-Mode Waves in the Earth's Inner Magnetosphere: Energy Distribution, Origins, and Role in Radiation Belt Dynamics. *Space Sci. Rev.* 200, 261–355. doi:10.1007/s11214-016-0252-5
- Artemyev, A. V., and Mourenas, D. (2020). On Whistler Mode Wave Relation to Electron Field-Aligned Plateau Populations. *J. Geophys. Res. Space Phys.* 125, e27735. doi:10.1029/2019JA027735
- Artemyev, A. V., Neishtadt, A. I., Vasiliev, A. A., and Mourenas, D. (2018). Long-term Evolution of Electron Distribution Function Due to Nonlinear Resonant Interaction with Whistler Mode Waves. *J. Plasma Phys.* 84, 905840206. doi:10.1017/S0022377818000260
- Blake, J. B., Looper, M. D., Baker, D. N., Nakamura, R., Klecker, B., and Hovestadt, D. (1996). New High Temporal and Spatial Resolution Measurements by Sampex of the Precipitation of Relativistic Electrons. *Adv. Space Res.* 18, 171–186. doi:10.1016/0273-1177(95)00969-8
- Blake, J. B., and O'Brien, T. P. (2016). Observations of Small-scale Latitudinal Structure in Energetic Electron Precipitation. *J. Geophys. Res. Space Phys.* 121, 3031–3035. doi:10.1002/2015JA021815

FUNDING

This work at UTD was supported by the NASA grants 80NSSC18K1224, 80NSSC19K0282, 80NSSC19K0283, 80NSSC21K0728, and 80NSSC21K1320. XZ and AA were supported by NSF grant 1914594. RH was supported by NERC Highlight Topic Grant NE/P01738X/1 (Rad-Sat) and NERC grant NE/V00249X/1 (Sat-Risk).

SUPPLEMENTARY MATERIAL

The Supplementary Material for this article can be found online at: <https://www.frontiersin.org/articles/10.3389/fspas.2021.745927/full#supplementary-material>

- Bortnik, J., Chen, L., Li, W., Thorne, R. M., and Horne, R. B. (2011). Modeling the Evolution of Chorus Waves into Plasmaspheric Hiss. *J. Geophys. Res.* 116, a–n. doi:10.1029/2011JA016499
- Breneman, A. W., Crew, A., Sample, J., Klumpar, D., Johnson, A., Agapitov, O., et al. (2017). Observations Directly Linking Relativistic Electron Microbursts to Whistler Mode Chorus: Van Allen Probes and Firebird II. *Geophys. Res. Lett.* 44, 11,265–11,272. doi:10.1002/2017GL075001
- Burtis, W. J., and Helliwell, R. A. (1969). Banded Chorus—A New Type of VLF Radiation Observed in the Magnetosphere by OGO 1 and OGO 3. *J. Geophys. Res.* 74, 3002–3010. doi:10.1029/JA074i011p03002
- Burton, R. K., and Holzer, R. E. (1974). The Origin and Propagation of Chorus in the Outer Magnetosphere. *J. Geophys. Res.* 79, 1014–1023. doi:10.1029/ja079i007p01014
- Chang, H. C., and Inan, U. S. (1983). A Theoretical Model Study of Observed Correlations between Whistler Mode Waves and Energetic Electron Precipitation Events in the Magnetosphere. *J. Geophys. Res.* 88, 10053–10064. doi:10.1029/ja088ia12p10053
- Chen, L., Bortnik, J., Li, W., Thorne, R. M., and Horne, R. B. (2012). Modeling the Properties of Plasmaspheric Hiss: 1. Dependence on Chorus Wave Emission. *J. Geophys. Res.* 117, 1. doi:10.1029/2011JA017201
- Chen, L., Breneman, A. W., Xia, Z., and Zhang, X.-j. (2020). Modeling of Bouncing Electron Microbursts Induced by Ducted Chorus Waves. *Geophys. Res. Lett.* 47, e2020GL089400. doi:10.1029/2020GL089400
- Chen, L., Thorne, R. M., Li, W., and Bortnik, J. (2013a). Modeling the Wave Normal Distribution of Chorus Waves. *J. Geophys. Res. Space Phys.* 118, 1074–1088. doi:10.1029/2012ja018343
- Chen, L., Thorne, R. M., Shprits, Y., and Ni, B. (2013b). An Improved Dispersion Relation for Parallel Propagating Electromagnetic Waves in Warm Plasmas: Application to Electron Scattering. *J. Geophys. Res. Space Phys.* 118, 2185–2195. doi:10.1002/jgra.50260
- Colpitts, C., Miyoshi, Y., Kasahara, Y., Delzanno, G. L., Wygant, J. R., Cattell, C. A., et al. (2020). First Direct Observations of Propagation of Discrete Chorus Elements from the Equatorial Source to Higher Latitudes, Using the Van Allen Probes and Arase Satellites. *J. Geophys. Res. Space Phys.* 125, e2020JA028315. doi:10.1029/2020JA028315
- Crew, A. B., Spence, H. E., Blake, J. B., Klumpar, D. M., Larsen, B. A., O'Brien, T. P., et al. (2016). First Multipoint *In Situ* Observations of Electron Microbursts: Initial Results from the Nsf Firebird II mission. *J. Geophys. Res. Space Phys.* 121, 5272–5283. doi:10.1002/2016JA022485
- Douma, E., Rodger, C. J., Blum, L. W., and Clilverd, M. A. (2017). Occurrence Characteristics of Relativistic Electron Microbursts from Sampex Observations. *J. Geophys. Res. Space Phys.* 122, 8096–8107. doi:10.1002/2017JA024067
- Furuya, N., Omura, Y., and Summers, D. (2008). Relativistic Turning Acceleration of Radiation Belt Electrons by Whistler Mode Chorus. *J. Geophys. Res.* 113, doi:10.1029/2007ja012478
- Gao, X., Mourenas, D., Li, W., Artemyev, A. V., Lu, Q., Tao, X., et al. (2016). Observational Evidence of Generation Mechanisms for Very Oblique Lower Band Chorus Using Themis Waveform Data. *J. Geophys. Res. Space Phys.* 121, 6732–6748. doi:10.1002/2016JA022915

- Hikishima, M., Omura, Y., and Summers, D. (2010). Microburst Precipitation of Energetic Electrons Associated with Chorus Wave Generation. *Geophys. Res. Lett.* 37, a–n. doi:10.1029/2010GL042678
- Horne, R. B., Glauert, S. A., and Thorne, R. M. (2003). Resonant Diffusion of Radiation Belt Electrons by Whistler-Mode Chorus. *Geophys. Res. Lett.* 30, 1. doi:10.1029/2003gl016963
- Horne, R. B. (1989). Path-integrated Growth of Electrostatic Waves: The Generation of Terrestrial Myriametric Radiation. *J. Geophys. Res.* 94, 895–909. doi:10.1029/ja094ia07p08895
- Imhof, W. L., Voss, H. D., Mobilia, J., Datlowe, D. W., Gaines, E. E., McGlennon, J. P., et al. (1992). Relativistic Electron Microbursts. *J. Geophys. Res.* 97, 13829–13837. doi:10.1029/92JA01138
- Katoh, Y., and Omura, Y. (2007). Relativistic Particle Acceleration in the Process of Whistler-Mode Chorus Wave Generation. *Geophys. Res. Lett.* 34, 1. doi:10.1029/2007gl031335
- Katoh, Y., and Omura, Y. (2006). Simulation Study on Nonlinear Frequency Shift of Narrow Band Whistler-Mode Waves in a Homogeneous Magnetic Field. *Earth Planet. Sp* 58, 1219–1225. doi:10.1186/BF03352013
- Kennel, C. F., and Petschek, H. E. (1966). Limit on Stably Trapped Particle Fluxes. *J. Geophys. Res.* 71, 1–28. doi:10.1029/jz071i001p00001
- Kersten, K., Cattell, C. A., Breneman, A., Goetz, K., Kellogg, P. J., Wygant, J. R., et al. (2011). Observation of Relativistic Electron Microbursts in Conjunction with Intense Radiation Belt Whistler-Mode Waves. *Geophys. Res. Lett.* 38, 1. doi:10.1029/2011gl046810
- Lam, M. M., Horne, R. B., Meredith, N. P., Glauert, S. A., Moffat-Griffin, T., and Green, J. C. (2010). Origin of Energetic Electron Precipitation >30 KeV into the Atmosphere. *J. Geophys. Res.* 115, a–n. doi:10.1029/2009JA014619
- Lampton, M. (1967). Daytime Observations of Energetic Auroral-Zone Electrons. *J. Geophys. Res.* 72, 5817–5823. doi:10.1029/JZ072i023p05817
- Lauben, D. S., Inan, U. S., Bell, T. F., and Gurnett, D. A. (2002). Source Characteristics of ELF/VLF Chorus. *J. Geophys. Res.* 107, 1429. doi:10.1029/2000ja003019
- LeDocq, M. J., Gurnett, D. A., and Hospodarsky, G. B. (1998). Chorus Source Locations from VLF Poynting Flux Measurements with the Polar Spacecraft. *Geophys. Res. Lett.* 25, 4063–4066. doi:10.1029/1998GL900071
- Li, W., Mourenas, D., Artemyev, A. V., Bortnik, J., Thorne, R. M., Kletzing, C. A., et al. (2016a). Unraveling the Excitation Mechanisms of Highly Oblique Lower Band Chorus Waves. *Geophys. Res. Lett.* 43, 8867–8875. doi:10.1002/2016gl070386
- Li, W., Santolik, O., Bortnik, J., Thorne, R. M., Kletzing, C. A., Kurth, W. S., et al. (2016b). New Chorus Wave Properties Near the Equator from Van Allen Probes Wave Observations. *Geophys. Res. Lett.* 43, 4725–4735. doi:10.1002/2016GL068780
- Li, W., Thorne, R. M., Angelopoulos, V., Bortnik, J., Cully, C. M., Ni, B., et al. (2009). Global Distribution of Whistler-Mode Chorus Waves Observed on the THEMIS Spacecraft. *Geophys. Res. Lett.* 36, L09104. doi:10.1029/2009GL037595
- Li, W., Thorne, R. M., Bortnik, J., Shprits, Y. Y., Nishimura, Y., Angelopoulos, V., et al. (2011a). Typical Properties of Rising and Falling Tone Chorus Waves. *Geophys. Res. Lett.* 38, a–n. doi:10.1029/2011GL047925
- Liu, X., Gu, W., Xia, Z., Chen, L., and Horne, R. B. (2021). Frequency-Dependent Modulation of Whistler-Mode Waves by Density Irregularities during the Recovery Phase of a Geomagnetic Storm. *Geophys. Res. Lett.* 48, e2021GL093095. doi:10.1029/2021GL093095
- Lorentzen, K. R., Blake, J. B., Inan, U. S., and Bortnik, J. (2001). Observations of Relativistic Electron Microbursts in Association with VLF Chorus. *J. Geophys. Res.* 106, 6017–6027. doi:10.1029/2000JA003018
- Lu, Q., Ke, Y., Wang, X., Liu, K., Gao, X., Chen, L., et al. (2019). Two-Dimensional gcPIC Simulation of Rising-Tone Chorus Waves in a Dipole Magnetic Field. *J. Geophys. Res. Space Phys.* 124, 4157–4167. doi:10.1029/2019JA026586
- Ma, Q., Artemyev, A. V., Mourenas, D., Li, W., Thorne, R. M., Kletzing, C. A., et al. (2017). Very Oblique Whistler Mode Propagation in the Radiation Belts: Effects of Hot Plasma and Landau Damping. *Geophys. Res. Lett.* 44, 057–066. doi:10.1002/2017GL075892
- Meredith, N. P., Horne, R. B., Sicard-Piet, A., Boscher, D., Yearby, K. H., Li, W., et al. (2012). Global Model of Lower Band and Upper Band Chorus from Multiple Satellite Observations. *J. Geophys. Res.* 117, A10225. doi:10.1029/2012ja017978
- Millan, R. M., and Thorne, R. M. (2007). Review of Radiation Belt Relativistic Electron Losses. *J. Atmos. Solar-Terrestrial Phys.* 69, 362–377. doi:10.1016/j.jastp.2006.06.019
- Millan, R. M. (2011). Understanding Relativistic Electron Losses with Barrel. *J. Atmos. Solar-Terrestrial Phys.* 73, 1425–1434. doi:10.1016/j.jastp.2011.01.006
- Ni, B., Thorne, R. M., Shprits, Y. Y., Orlova, K. G., and Meredith, N. P. (2011). Chorus-driven Resonant Scattering of Diffuse Auroral Electrons in Nondipolar Magnetic Fields. *J. Geophys. Res.* 116, a–n. doi:10.1029/2011JA016453
- Nishimura, Y., Bortnik, J., Li, W., Liang, J., Thorne, R. M., Angelopoulos, V., et al. (2015). Chorus Intensity Modulation Driven by Time-varying Field-aligned Low-energy Plasma. *J. Geophys. Res. Space Phys.* 120, 7433–7446. doi:10.1002/2015JA021330
- Nunn, D., Omura, Y., Matsumoto, H., Nagano, I., and Yagitani, S. (1997). The Numerical Simulation of VLF Chorus and Discrete Emissions Observed on the Geotail Satellite Using a Vlasov Code. *J. Geophys. Res.* 102, 27083–27097. doi:10.1029/97JA02518
- O'Brien, T. P., Looper, M. D., and Blake, J. B. (2004). Quantification of Relativistic Electron Microburst Losses during the Gem Storms. *Geophys. Res. Lett.* 31, 1. doi:10.1029/2003GL018621
- Oliven, M. N., and Gurnett, D. A. (1968). Microburst Phenomena: 3. An Association between Microbursts and VLF Chorus. *J. Geophys. Res.* 73, 2355–2362. doi:10.1029/JA073i007p02355
- Omura, Y., Hikishima, M., Katoh, Y., Summers, D., and Yagitani, S. (2009). Nonlinear Mechanisms of Lower-Band and Upper-Band VLF Chorus Emissions in the Magnetosphere. *J. Geophys. Res. Space Phys.* 114, 1. doi:10.1029/2009ja014206
- Omura, Y., and Matsumoto, H. (1982). Computer Simulations of Basic Processes of Coherent Whistler Wave-Particle Interactions in the Magnetosphere. *J. Geophys. Res.* 87, 4435–4444. doi:10.1029/ja087ia06p04435
- Omura, Y., Miyashita, Y., Yoshikawa, M., Summers, D., Hikishima, M., Ebihara, Y., et al. (2015). Formation Process of Relativistic Electron Flux through Interaction with Chorus Emissions in the Earth's Inner Magnetosphere. *J. Geophys. Res. Space Phys.* 120, 9545–9562. doi:10.1002/2015JA021563
- Omura, Y., and Summers, D. (2006). Dynamics of High-Energy Electrons Interacting with Whistler Mode Chorus Emissions in the Magnetosphere. *J. Geophys. Res.* 111, 1. doi:10.1029/2006JA011600
- Parks, G. K., Gurgiolo, C., and West, R. (1979). Relativistic Electron Precipitation. *Geophys. Res. Lett.* 6, 393–396. doi:10.1029/GL006i005p00393
- Reeves, G. D., Spence, H. E., Henderson, M. G., Morley, S. K., Friedel, R. H. W., Funsten, H. O., et al. (2013). Electron Acceleration in the Heart of the Van Allen Radiation Belts. *Science* 341, 991–994. doi:10.1126/science.1237743
- Rosenberg, T. J., Wei, R., Detrick, D. L., and Inan, U. S. (1990). Observations and Modeling of Wave-Induced Microburst Electron Precipitation. *J. Geophys. Res.* 95, 6467–6475. doi:10.1029/JA095iA05p06467
- Saito, S., Miyoshi, Y., and Seki, K. (2012). Relativistic Electron Microbursts Associated with Whistler Chorus Rising Tone Elements: Gemis-Rbw Simulations. *J. Geophys. Res.* 117, a–n. doi:10.1029/2012JA018020
- Santolik, O., Gurnett, D. A., Pickett, J. S., Parrot, M., and Cornilleau-Wehrlin, N. (2005). Central Position of the Source Region of Storm-Time Chorus. *Planet. Space Sci.* 53, 299–305. doi:10.1016/j.pss.2004.09.056
- Santolik, O., and Gurnett, D. A. (2003). Transverse Dimensions of Chorus in the Source Region. *Geophys. Res. Lett.* 30. doi:10.1029/2002GL016178
- Shen, X. C., Li, W., Ma, Q., Agapitov, O., and Nishimura, Y. (2019). Statistical Analysis of Transverse Size of Lower Band Chorus Waves Using Simultaneous Multisatellite Observations. *Geophys. Res. Lett.* 46, 5725–5734. doi:10.1029/2019gl083118
- Shprits, Y. Y., and Ni, B. (2009). Dependence of the Quasi-Linear Scattering Rates on the Wave Normal Distribution of Chorus Waves. *J. Geophys. Res.* 114, a–n. doi:10.1029/2009JA014223
- Shumko, M., Johnson, A. T., Sample, J. G., Griffith, B. A., Turner, D. L., O'Brien, T. P., et al. (2020). Electron Microburst Size Distribution Derived with Aerocube-6. *J. Geophys. Res. Space Phys.* 125, e2019JA027651. doi:10.1029/2019JA027651

- Shumko, M., Sample, J., Johnson, A., Blake, B., Crew, A., Spence, H., et al. (2018). Microburst Scale Size Derived from Multiple Bounces of a Microburst Simultaneously Observed with the Firebird-Ii Cubesats. *Geophys. Res. Lett.* 45, 8811–8818. doi:10.1029/2018gl078925
- Smith, R. L., Helliwell, R. A., and Yabroff, I. W. (1960). A Theory of Trapping of Whistlers in Field-Aligned Columns of Enhanced Ionization. *J. Geophys. Res.* 65, 815–823. doi:10.1029/JZ065i003p00815
- Tao, X. (2014). A Numerical Study of Chorus Generation and the Related Variation of Wave Intensity Using the Dawn Code. *J. Geophys. Res. Space Phys.* 119, 3362–3372. doi:10.1002/2014JA019820
- Tao, X., and Bortnik, J. (2010). Nonlinear Interactions between Relativistic Radiation Belt Electrons and Oblique Whistler Mode Waves. *Nonlin. Process. Geophys.* 17, 599–604. doi:10.5194/npg-17-599-2010
- Tao, X., Bortnik, J., Thorne, R. M., Albert, J. M., and Li, W. (2012). Effects of Amplitude Modulation on Nonlinear Interactions between Electrons and Chorus Waves. *Geophys. Res. Lett.* 39, a–n. doi:10.1029/2012GL051202
- Teng, S., Tao, X., Xie, Y., Zonca, F., Chen, L., Fang, W. B., et al. (2017). Analysis of the Duration of Rising Tone Chorus Elements. *Geophys. Res. Lett.* 44, 074–082. doi:10.1002/2017GL075824
- Thorne, R. M., Li, W., Ni, B., Ma, Q., Bortnik, J., Chen, L., et al. (2013). Rapid Local Acceleration of Relativistic Radiation-belt Electrons by Magnetospheric Chorus. *Nature* 504, 411–414. doi:10.1038/nature12889
- Tsurutani, B. T., and Smith, E. J. (1974). Postmidnight Chorus: A Substorm Phenomenon. *J. Geophys. Res.* 79, 118–127. doi:10.1029/JA079i001p00118
- Tyler, E., Breneman, A., Cattell, C., Wygant, J., Thaller, S., and Malaspina, D. (2019). Statistical Distribution of Whistler Mode Waves in the Radiation Belts with Large Magnetic Field Amplitudes and Comparison to Large Electric Field Amplitudes. *J. Geophys. Res. Space Phys.* 124, 6541–6552. doi:10.1029/2019JA026913
- Watt, C. E. J., Degeling, A. W., and Rankin, R. (2013). Constructing the Frequency and Wave Normal Distribution of Whistler-Mode Wave Power. *J. Geophys. Res. Space Phys.* 118, 1984–1991. doi:10.1002/jgra.50231
- Zhang, X.-J., Thorne, R., Artemyev, A., Mourenas, D., Angelopoulos, V., Bortnik, J., et al. (2018). Properties of Intense Field-Aligned Lower-Band Chorus Waves: Implications for Nonlinear Wave-Particle Interactions. *J. Geophys. Res. Space Phys.* 123, 5379–5393. doi:10.1029/2018JA025390
- Zheng, L., Chen, L., and Zhu, H. (2019). Modeling Energetic Electron Nonlinear Wave-Particle Interactions with Electromagnetic Ion Cyclotron Waves. *J. Geophys. Res. Space Phys.* 124, 3436–3453. doi:10.1029/2018JA026156

Conflict of Interest: The authors declare that the research was conducted in the absence of any commercial or financial relationships that could be construed as a potential conflict of interest.

Publisher's Note: All claims expressed in this article are solely those of the authors and do not necessarily represent those of their affiliated organizations, or those of the publisher, the editors and the reviewers. Any product that may be evaluated in this article, or claim that may be made by its manufacturer, is not guaranteed or endorsed by the publisher.

Copyright © 2021 Chen, Zhang, Artemyev, Zheng, Xia, Breneman and Horne. This is an open-access article distributed under the terms of the Creative Commons Attribution License (CC BY). The use, distribution or reproduction in other forums is permitted, provided the original author(s) and the copyright owner(s) are credited and that the original publication in this journal is cited, in accordance with accepted academic practice. No use, distribution or reproduction is permitted which does not comply with these terms.